The Multislice Method in Transmission Electron Microscopy Simulation

An implementation in the TEM-simulator software package

ALI NARANGIFARD



Master's Degree Project Stockholm 2013

TRITA-STH EX 2013:101

The Multislice Method in Transmission Electron Microscopy Simulation

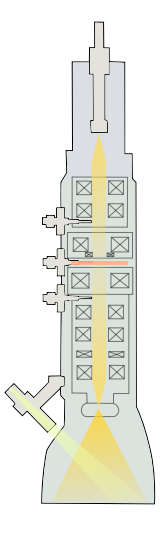
Ali Narangifard

Master of Science Thesis in Medical Imaging Advanced level (second cycle), 30 credits Supervisors at KTH: Ozan Öktem and Philip Köck Examiner: Hans Hebert School of Technology and Health TRITA-STH EX 2013:101

> Royal Institute of Technology KTH STH SE-141 86 Flemingsberg, Sweden http://www.kth.se/sth

Abstract

This report introduces the multislice method for modeling the interaction between an electron and the atoms in the specimen (electron-specimen interaction). The multislice method is an approximation to the full quantum mechanical model for this interaction. After introducing the theory, we discuss how the multislice method is implemented and integrated into TEM-simulator, a software for simulation of Transmission Electron Microscope (TEM) images.



Referat

Implementation av multislice metoden för simulering av transmissionselektronmikroskopi

Denna rapport presenterar multislice-metoden som används till att modellera interaktionen mellan en elektron och atomerna i ett prov (elektron-prov-interaktion). Multislice-metoden är en approximation till den fullständiga kvantmekaniska modellen för denna interaktion. Efter införandet av teorin diskuterar vi hur multislice-metoden implementeras och integreras i TEM-simulator, en programvara för simulering av Transmission Elektron Mikroskop (TEM) bilder.

Acknowledgments

Foremost I would like to express my sincere appreciation toward Dr. Philip Köck to whom I owe the indispensable knowledge of this thesis and Dr. Ozan Öktem whose guidance and contribution have been elemental constituents of this work.

I am also immensely grateful to my friends in Stockholm for their vital and persistent support.

And finally I owe my family a great debt of gratitude for providing me with the most crucial necessities throughout the life and education.

Contents

Contents

1	Intr	oduction	n	1					
2	Phy	ysics of Image Formation							
	2.1	Electron	n source	7					
	2.2	Electron	n-specimen interaction	8					
		2.2.1	Specimen model	8					
		2.2.2	Approximations	9					
		2.2.3	Γhe multislice method	10					
	2.3	Optics		10					
	2.4	Detector	r	11					
3	Elec	ctron-Sp	ecimen Model	13					
	3.1	The Sch	rödinger equation in the stationary setting	13					
	3.2	Comput	ational models for the electron-specimen interaction	14					
	3.3	The mu	ltislice method	15					
	3.4								
			Electrons that mainly propagate along a fixed direction	16					
		3.4.2 I	Free space propagation	17					
		3.4.3	The multislice equation	20					
4 I	Imp	olementa	ation	23					
	4.1	The par	ts of the TEM-simulator	23					
		4.1.1 H	Phantom generator	23					
			ΓΕM simulator	24					
	4.2		the multislice method	25					
		4.2.1 V	Wave function	25					
			Generating slices	25					
			Propagation	26					
			Transmission	27					
			Optics and Detectors	28					
	4.3	Modifica	ations in TEM-Simulator	28					

5	Results	31
Bi	bliography	35

Chapter 1

Introduction

Since its introduction in the early 1600's, microscopy is an essential part of scientific discovery, and especially so in life sciences. From then on, there has been tremendous technical and scientific development, e.g. in the understanding of the wave/particle nature of light, design of optics, and precision engineering.

German physicist Ernst Abbe laid the foundation of modern optics and established a formula describing the resolving power of a microscope in terms of the wavelength and numerical aperture of the optical system. Another breakthrough came with Frits Zernike, a Dutch physicist, who invented the phase contrast microscope. This permits the study of sub-cellular structures without the need to stain, hence one could now study live cells. Zernike was awarded the Nobel prize (physics) in 1953 for the discovery of phase contrast microscopy.

The next major development for light microscopy came with the discovery of green fluorescent protein in a jellyfish species by Osamu Shimomura in 1961. This marked the beginning of fluorescence microscopy, an optical microscopy modality that uses fluorescence and phosphorescence instead of, or in addition to, reflection and absorption of

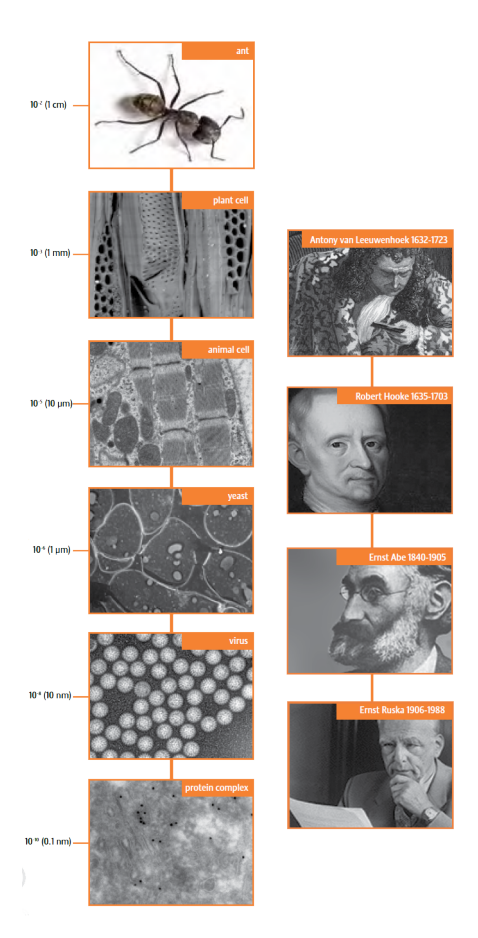


Figure 1.1. Evolution of resolution in microscopy.

light to study properties of organic or inorganic substances. Coupled with the devel-

opment of high-resolution microscopes, fluorescence microscopy is now a mainstream tool, bringing about a revolution for biological imaging, and having a profound impact on the way research is being conducted in the life sciences.

Quest for higher resolution The notion of "image quality" is complex and highly task dependent. Still, there are three components that often play a central role in obtaining a good image: contrast, resolving power and magnification. Abbe's above mentioned formula made it clear that the resolving power is ultimately limited by the wavelength. The resolving power of light microscopy is therefore always limited by the wavelength of visible light. One line of development to increase the resolving power is to design microscopy that operates using light (photons) with shorter wavelengths than visible light. The difficulty here is to design optical elements (lenses, mirrors, etc.) that can focus and reflect such x-ray photons. There are now some prototype microscopes (soft x-ray microscopes) that operate using electromagnetic waves in the x-ray regime, but this is still very much work in progress.

Another line of development came with the quantum mechanical understanding of the wave/particle duality of matter. In 1924, Louis de Broglie introduced the concept of matter waves, later perfected by George Thomson and Clinton Davisson. In 1926, Erwin Schrödinger published his by now famous equation, the Schrödinger equation, modelling the evolution of matter waves. This opened up for the idea of using electrons instead of light in microscopes. The benefit was that appropriately accelerated electrons have a wavelength significantly lower than visible light. Furthermore, since electrons are charged particles, they can be manipulated using electric or magnetic fields. This makes it possible to design electron optical elements that mimic the effect of optical lenses in light microscopy, see figure 1.2. Exploiting these characteristics, in 1928 Ernst Ruska began working on electron lenses and in 1931 he built the first electron microscope at the University of Berlin. For this, he was awarded the Nobel prize in physics in 1986. Below we provide a very brief summary of the development of electron microscopy, see [14] for further details.

Following the discovery in 1931 by Ruska, further prototype electron microscope were built, mostly for examining the effects on images of different magnetic and electrostatic lenses. In 1933 the first electron microscope image of a biological specimen was obtained by Marton using a three-lens electron microscope. Later, in 1938 Hiller and Prebus they built an electron microscope with 6 nm resolution and 40,000× magnification. In 1939 Siemens delivers the first commercial TEM in serial production and other companies entered this contest soon after. Current electron microscopes use a third magnetic lens and their resolution reaches 0.05 nm, about 4000 times better than a typical light microscope. Alongside the technological development, there has also been effort in developing mathematical models for the different parts of electron microscopy imaging. One notable event is from 1957 when John Cowley and Alexander Moodie introduced the multislice method for modeling electron-specimen interactions. Another is from 1965 when Karl-Joseph

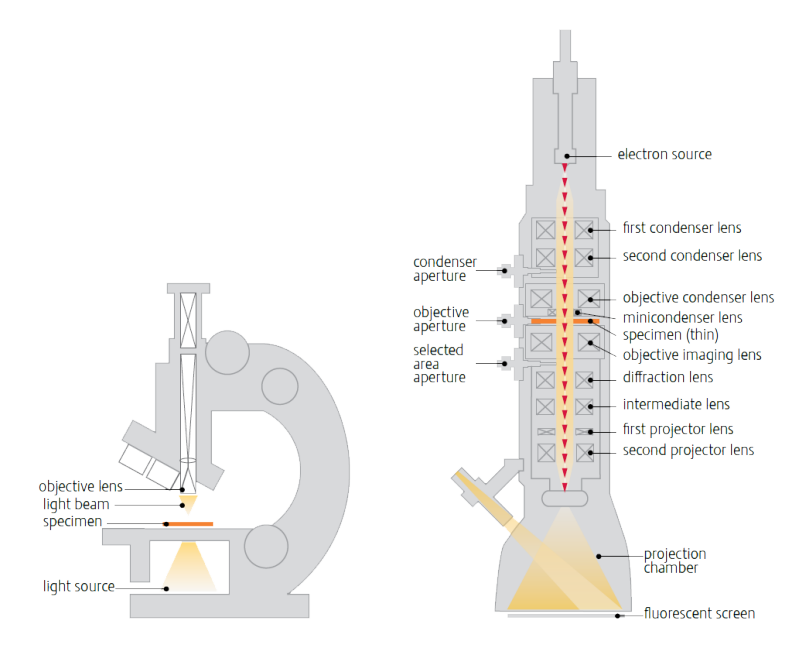
Hanszen introduces contrast transfer function for modeling the effects of the lenses in electron microscopes.

Specimen preparations have also been a central issue, especially for imaging biological specimens. The specimen needs to be solidified (fixation) and it also needs to be protected from degradation caused by interaction with high energy electrons. All this is to be done while preserving the structural integrity of the specimen. One approach for fixation is low-temperature methods, introduced in 1951 to study biological membranes by Humberto Fernández-Morán. This method later evolved into cryo-electron microscopy, which is widely used today for single particle microscopy. In 1955, Cecil Hall published a study of the effect of various staining methods on viruses, and described viral particles that were not positively stained by phosphotungstic acid, but appeared to be embedded in the dried reagent and displayed a negative contrast. Since then, negative staining is used for increasing the contrast and preserving the specimen.

Usage of electron microscopy Electron microscopes constitute an indispensable part of basic physics research, e.g. in material sciences TEMs are used to characterise materials down to the atomic level. Electron microscopes are also extensively used in semiconductor industry.

Regarding life sciences, one of the main goals for present-day electron microscopy is to look at the life processes within a cell at the molecular level. During recent years electron microscopy has developed into a most useful tool to study macromolecules, molecular complexes and supramolecular assemblies in three dimensions (3D electron microscopy). Three main techniques have been applied: electron crystallography reviewed in [16, 11], single particle analysis reviewed in [9], and electron tomography reviewed in [24, 26, 21]. Electron crystallography permits structural analysis of macromolecules at or close to atomic resolution (0.4 nm or better). It relies on the availability of 2D crystals and has proven especially suited for membrane proteins. Larger biological complexes are preferably studied by single particle analysis, which in favourable cases allows the molecular objects to be examined at medium-resolution (1-2 nm). Notably, this resolution is good enough to permit high-resolution structures of subunits or domains (usually obtained by X-ray crystallography) to be fitted into the large structure at hand. This hybrid approach may reveal the entire complex at close to atomic resolution. Finally, electron tomography can provide structural information at the molecular level in the context of the cellular environment. Most importantly, small cells or sections through larger cells or tissues can be studied as cryospecimens with a close-to-life preservation as shown by [1, 21]. The resolution is presently limited to 4-5 nm but it seems reasonable to reach higher resolution in a near future. The docking approach would then be realistic, which will help identifying and characterising the molecular complexes observed. It should finally be recalled that electron tomography examines the supramolecular assemblies as individual objects. This is essential as within the cell these complex structures are likely to be dynamic, changing conformation and subunit composition, and interacting, often transiently, with other molecular assemblies and cellular structures. Thus, often in conjunction with other methods such as X-ray crystallography, mass spectrometry and single particle analysis, as shown in [28, 32], electron tomography is likely to be a most efficient tool to visualise the supramolecular structures at work, which will help us understanding how they operate within the cell at the molecular level.

Importance of an electron microscopy simulator Bearing in mind the above mentioned striking development and the future expected potential of 3D electron microscopy, it is anticipated that simulation of electron images will play an increasingly important role in future molecularly oriented electron microscopy. A molecular model (phantom), created by means of a phantom generator using information stored in databases, generator can together with a simulator be used for in silico electron microscopy imaging. Ideally, background variability and noise are also properly incorporated into the image. Such a tool will be valuable for identifying and characterising molecular objects in electron images of isolated objects as well as of objects in the cellular environment. Furthermore, a simulator is also necessary to easily and cost-efficiently test and evaluate the impact of new image processing methods as well as novel data collection techniques and improved instrumentation. Finally, a good simulator can be applied for educational purpose too, Since we can produce the expected image from a specific specimen in a specific condition.



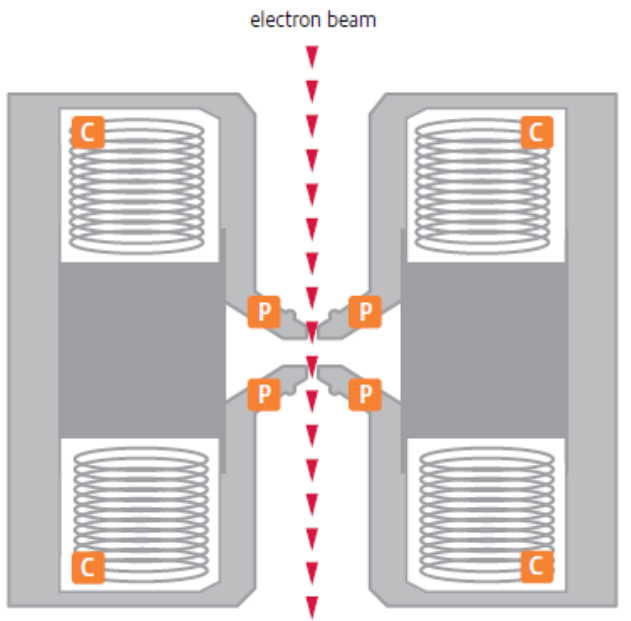


Figure 1.2. Upper image compares a light microscope to a TEM. Lower image shows a coss-section of an electromagnetic lens and the passage of electrons through its centre. Here, C is an electrical coil and P is the soft iron pole piece. Both figures are provided by FEI company $^{\text{TM}}$ with permission.

Chapter 2

Physics of Image Formation

This chapter reviews models describing the different parts of a TEM and their influence on the image formation. The image formation model naturally decomposes into the following:

Electron source: Model for the source emitting the imaging electrons.

Electron-specimen interaction: Model for the interaction between the imaging electrons and the atoms in the specimen.

Optics: Model for the TEM optics.

Detector: Model for the intensity formation and the TEM detector.

An important aspect in separately modelling such coupled phenomena is to make sure that the models use consistent assumptions. The underlying physics is here governed by quantum mechanics, where in the full model, both the imaging electron and specimen are given by their wave functions. We will however only treat the imaging electron quantum mechanically as a time harmonic wave:

$$\Psi(\mathbf{x},t) = \psi(\mathbf{x}) \exp(-iEt/\hbar)$$
 where E is the energy of the electron.

The spatial variation $\psi \colon \mathbb{R}^3 \to \mathbb{C}$ will be referred to as the *electron wave*.

In the subsections that follow, we provide a brief description of how each of the above parts are modelled given the above setting.

2.1 Electron source

In TEM imaging, the electrons used for imaging (imaging electrons) are first dispensed from an electron gun. Next, they pass through the condenser which is an optical system that provides *coherent illumination*. This refers to the situation when the imaging electrons can be described as monochromatic plane waves and it is highly desirable for a variety of reasons. Furthermore, the TEM needs to be

aligned in the sense that the imaging electrons travel along the TEM optical axis. In summary, as the imaging electron leaves the condenser, it is modelled as

$$\Psi_{\rm in}(\boldsymbol{x},t) = \exp(ik\boldsymbol{x}\cdot\boldsymbol{\omega})\exp(-iEt/\hbar)$$

where its direction of propagation ω is parallel to the TEM optical axis.

The above simply states that imaging electrons are plane waves traveling along the optical axis. In reality the illumination is of course not perfectly coherent. Partial incoherence introduced by the illumination is frequently modelled phenomenologically as a convolution with a rotation invariant filter that decreases exponentially in Fourier space as frequencies grow (envelope functions), see, e.g., [8, 7, 34].

2.2 Electron-specimen interaction

After leaving the condenser, the imaging electron scatters against the atoms in the specimen. The wave function for the scattered electron is given as the solution to the $Schr\"{o}dinger\ equation$

$$i\hbar\frac{\partial}{\partial t}\Psi(\boldsymbol{x},t) = \Big[-\frac{\hbar^2}{2m}\nabla^2 + V(\boldsymbol{x})\Big]\Psi(\boldsymbol{x},t).$$

In the above, V is the object function given by the interaction Hamiltonian, ∇^2 denotes the Laplacian in \mathbb{R}^3 , and m is the mass of the imaging electron.

One remark concerns how to account for relativistic effects. Under the conditions in TEM imaging, it is clear that relativistic effects cannot be ignored. The appropriate equation is the Dirac equation, but a computationally more feasible option is to use the Schrödinger equation with relativistically corrected electron mass and wavelength [10]. Hence, m above is the relativistically corrected mass of the electron.

2.2.1 Specimen model

The goal of the specimen model is to derive a computationally feasible model for the interaction Hamiltonian V, henceforth called the *object function*. The most common model is based on the isolated atom superposition approximation. Here, one considers the atoms in the specimen as isolated from each other. For a specimen where the nuclei of the j:th atoms is at x_j and its atomic number is Z_j , the object function is given by

$$V(oldsymbol{x}) = \sum_{j} V_{Z_j}(oldsymbol{x} - oldsymbol{x}_j).$$

In the above, $V_Z: \mathbb{R}^3 \to \mathbb{R}$ is the potential of an isolated atom centred at the origin with atomic number Z, so

$$V_Z(\boldsymbol{x} - \boldsymbol{x}_0) = rac{1}{4\pi\epsilon_0} \left[\int_{\mathbb{R}^3} rac{
ho_Z(\boldsymbol{y})}{|\boldsymbol{x} - \boldsymbol{y}|} \,\mathrm{d}\boldsymbol{y} - rac{eZ}{|\boldsymbol{x} - \boldsymbol{x}_0|}
ight]$$

2.2. ELECTRON-SPECIMEN INTERACTION

with $\rho_Z \colon \mathbb{R}^3 \to \mathbb{R}$ denoting the electron density function associated to the shell electrons of the isolated atom.

The isolated atom consists of a positively charged nucleus surrounded by a negatively charged electron cloud. The electric charges give rise to an electrostatic potential at a point in space whose three-dimensional Fourier transform is the (electron) scattering factor of the atom. Numerical values of the latter for all atoms of interest can be obtained from experiments and results are tabulated in the literature. This values take into account both elastic electron-cloud scattering ρ_Z and elastic nuclear scattering (from -eZ). Parameterisations can be found in [27, section 2.3 and appendix D].

The the isolated atom superposition approximation ignores the charge distribution associated with the chemical bonds. As atomic potentials provide the most significant contribution to the scattering of incident electron, this computationally feasible approximation provides an excellent starting point for initial interpretation of high-energy electron diffraction experiments. As a final note, one can also add an imaginary part to V to account for effects due to inelastic scattering:

$$V(oldsymbol{x}) = \sum_{j} V_{Z_j}(oldsymbol{x} - oldsymbol{x}_j) + i V_{Z_j}^{\mathrm{abs}}(oldsymbol{x} - oldsymbol{x}_j)$$

where $V_{Z_j}^{\text{abs}}$ is the absorption potential used for modelling the decrease in the flux, due to inelastic scattering, of the non-scattered and elastically scattered electrons [29].

2.2.2 Approximations

An issue related to calculating the scattered electron wave by solving the Schrödinger equation is that this is computationally intractable. Due to the small wavelength of the imaging electron, standard techniques from numerical analysis, like the finite element method, are out of the question for calculating the scattered electron wave, this even in cases when the specimen is very thin (say not more than 50 nm thick).

One option is to look for various approximations. One approximation is to assume that the electron wave essentially only undergoes a phase shift as it scatters against the specimen, which brings us to phase contrast imaging. It is a reasonable assumption for thin weakly scattering specimens and the amplitude term of the scattered wave

$$\psi_{\rm sc}(\boldsymbol{x}) = \tau(\boldsymbol{x})\psi_{\rm in}(\boldsymbol{x})$$

where ψ_{in} is the amplitude term of the incoming wave and the phase shift is given by

$$\tau(\boldsymbol{x}) := \exp\left(i\sigma \int_{-\infty}^{0} V(\boldsymbol{x} + s\boldsymbol{\omega}) \,\mathrm{d}s\right) \quad \text{with} \quad \sigma := \frac{me}{k\hbar^2}.$$

Note that V above is the complex-valued object function that models the influence of the specimen. In the weak phase approximation one makes one further

approximation, namely to take the Taylor expansion of the exponential in τ :

$$\psi_{\rm sc}(\boldsymbol{x}) \approx 1 + i\sigma \int_{-\infty}^{0} V(\boldsymbol{x} + s\boldsymbol{\omega}) \, \mathrm{d}s.$$

Hence, the projection of the object function along the propagation axis is enough for calculating the phase shift of the incoming electron wave. This gives us a linear relation between the object function and the scattered wave (note that in the initial model, the scattered electron wave depends non-linearly on the object function). Further details are given in section 3.1.

2.2.3 The multislice method

In thicker specimens there is diffraction along the propagation direction of the specimen and the effect of the object function at each point in the specimen is not independent from other points. Hence, contributions to the scattered electron cannot be added independently, so a linear model like the weak phase object model does not hold.

A more accurate model accounting for the above phenomena should refer to the physics of electrodynamics which describes the behaviour of a high energy electron scattering against atoms. One of the first attempts for this kind of electron-specimen modelling was made for crystallised specimens [4]. The approach, which later came to be known as the *multislice method*, was refined and some of its properties as an approximation method were studied in [13]. In the next chapter we will discuss this approximation in more detail.

2.3 Optics

After scattering against the specimen, the imaging electron passes through a number of magnetic lenses before reaching the detector. These lenses add some artefacts to the wave-function, e.g., aberrations and astigmatism. A common model is to assume that the optics is linear and translation invariant, in which case the influence of the optics can be modelled through a 2D convolution in the plane orthogonal to the optical axis [6, 15, 22, 33, 17]. The kernel for the convolution is referred to as the Point Spread Function (PSF) and it describes how a point source is smeared out due to the optics. In Fourier space this convolution turns into a multiplication and the Fourier transform of the PSF is called the Contrast Transfer Function (CTF) (or optical transfer function).

We now take a closer look at the PSF relevant for TEM imaging. Let ψ_{sc} denote the scattered electron wave function leaving the specimen. The wave function ψ_{det} for the electron immediately before it reaches the detector can then be expressed as [30]

$$\widehat{\psi}_{\text{det}}(\boldsymbol{\xi}) = \widehat{\psi}_{\text{sc}}(\boldsymbol{\xi}) \exp(-i\chi(\boldsymbol{\xi})).$$

2.4. DETECTOR

In the above, $\hat{\psi}_{sc}$ and $\hat{\psi}_{det}$ are the 2D Fourier transforms of ψ_{sc} and ψ_{det} in the plane orthogonal to the optical axis, respectively. Also,

$$\chi(\boldsymbol{\xi}) := \frac{2\pi}{\lambda} \left(\frac{1}{4} C_s \lambda^4 |\boldsymbol{\xi}|^4 - \frac{1}{2} \Delta f \lambda^2 |\boldsymbol{\xi}|^2 \right)$$

where C_s and spherical aberration and Δf is the defocus value [35, 20].

2.4 Detector

After passing through the optics, the imaging electron hits the detector. The first thing that happens is that an intensity is generated. All detectors are based on measuring this intensity. A common detector type ha a scintillator crystal coupled with a CCD camera. The scintillator trades the energy of the high energy imaging electrons to photons detectable by a CCD. Such a detector introduces a dispersion effect to the intensity which can be modelled with a 2D low pass filter in the detector plane given by a convolution with kernel h_{det} :

$$I(\boldsymbol{x}) = \left|\psi_{\text{det}}(\boldsymbol{x})\right|^2 \otimes h_{\text{det}}(\boldsymbol{x}).$$

Note that the convolution \otimes above is a 2D convolution in the detector plane, the latter almost always taken as orthogonal to the optical axis. The CCD camera consists of a dense grid of sensors, each measuring the number of photons reached to it from scintillator. This introduces two dimensional sampling of the out-coming wave's intensity. Note also that the detector adds noise to the measured signal.

Chapter 3

Electron-Specimen Model

The objective in this chapter is to arrive at the multislice approximation useful for simulating electron-specimen interactions in TEM imaging.

3.1 The Schrödinger equation in the stationary setting

As already mentioned, the wave function Ψ of the scattered imaging electron fulfils the scalar Schrödinger equation

$$i\hbar rac{\partial}{\partial t} \Psi(m{x},t) = \Big[-rac{\hbar^2}{2m}
abla^2 + V(m{x}) \Big] \Psi(m{x},t)$$

where V is the object function given by the interaction Hamiltonian, ∇^2 denotes the Laplacian in \mathbb{R}^3 , and m is the relativistically corrected mass of the imaging electron. Furthermore, the electron wave function is time harmonic and of the form

$$\Psi(\mathbf{x},t) = \psi(\mathbf{x}) \exp(-iEt/\hbar)$$
 where E is the total energy.

Now, the potential energy is negligible compared the kinetic energy of the imaging electron, so the total energy E can be taken to be equal to the kinetic energy of imaging electron. Hence, $E=k^2\hbar^2/2m$ where the wavenumber $k:=2\pi/\lambda$ depends on the relativistically corrected wavelength λ . We then arrive at the following Helmholtz type of equation for ψ :

$$E\psi(\mathbf{x}) = \left[-\frac{\hbar^2}{2m} \nabla^2 - eV(\mathbf{x}) \right] \psi(\mathbf{x}). \tag{3.1}$$

We will also make use of the scattering potential which is defined as

$$U(\boldsymbol{x}) := \frac{2em}{\hbar^2} V(\boldsymbol{x}) \quad \text{for } \boldsymbol{x} \in \mathbb{R}^3.$$
 (3.2)

Then, (3.1) simplifies to

$$k^{2}\psi(\boldsymbol{x}) = -\left[\nabla^{2} + U(\boldsymbol{x})\right]\psi(\boldsymbol{x}). \tag{3.3}$$

Furthermore, we note that

$$\frac{1}{2k} \int U(\boldsymbol{x} + s\boldsymbol{\omega}) \, ds = \sigma \int V(\boldsymbol{x} + s\boldsymbol{\omega}) \, ds$$

where $\sigma := 2\pi m\lambda e/h^2$ (with $h = 2\pi\hbar$), usually called the *interaction parameter*, and $k = 2\pi/\lambda$ is the wave number of the electron (λ is the electron wavelength).

As a final note, the scattering potential U can also be extended to include "absorption" by adding an imaginary part, so we will assume that $U: \mathbb{R}^3 \to \mathbb{C}$. The calculation of scattering potential from a specification of the specimen is taken care of by the TEM-simulator [29].

3.2 Computational models for the electron-specimen interaction

The wavelength of a 200 keV electron is 0.0025 nm. A straightforward numerical sampling of this wavelength for solving the partial differential equation (3.1) would require of order 10 points per wavelength. To sample a small specimen in a cube of 10 nm per side would require about $(10 \cdot 10/0.0025)^3 \approx 6.4 \cdot 10^{13}$ points. Even in single precision (four bytes per value) this would require $2.4 \cdot 10^5$ Gbytes of memory, which is clearly not possible in the near future. Clearly some other approach must be found.

There are two principle means of calculating the propagation of the electrons through a specimen transmission, the Bloch wave method and the multislice method.

Bloch wave: The electron wave function is expanded in Bloch waves inside a crystalline specimen, which have the periodicity of the specimen and satisfy the Schrödinger equation. Requires finding the Eigenvectors and values of a large matrix. Good for small perfect crystals but the computer time scales as N^3 where N is the number of Bloch waves or Fourier components (N increases with resolution).

Multislice: Divide the specimen into many thin slices. Alternately transmit and propagate the slowly varying portion of the wave function through the specimen. Will work on crystalline or nearly amorphous specimens. Using an efficient Fourier transform, e.g. Fast Fourier Transform (FFT), the computer time scales approximately as $N \log(N)$ where N is the number of Fourier components (N increases with resolution).

The Bloch wave approach is described in several books, e.g., [5], and will not be discussed in detail here since it only applies to crystalline specimens. The multislice method was first described in [4] and later expanded in [13]. The FFT was first added in [19] and [3] greatly improved the computational efficiency (reduces CPU time) of the multislice method. The FFT based multislice method is presented in [20] and will be discussed briefly below. See also [12] for simulation of general objects by means of multislice.

3.3 The multislice method

The multislice method solves the above sampling problem by factoring the electron wave function into a part that varies with the wavelength and a slowly varying portion that is sampled in real space at a much larger sample spacing (because the specimen has only a small effect on the scale of the electron wavelength).

Consider an electron traveling in the ω -direction in \mathbb{R}^3 (usually the directional vector ω is parallel to the optical axis of the TEM). Then, the corresponding electron wave function ψ can be written as

$$\psi(\mathbf{x}) = \phi(\mathbf{x}) \exp(ik\mathbf{x} \cdot \boldsymbol{\omega}) \tag{3.4}$$

where ϕ is the slowly varying portion of the wave function.

Insert (3.4) into (3.1) and solve for ϕ , the slowly varying portion of the wave function. Note here that the sampling of the slowly varying portion ϕ may be spaced many wavelengths apart. This approximation is justified because the incident electron beam is a relatively high energy and is not changed significantly on the scale of its wavelength. Back scattered waves are also neglected.

Another approximation in the multislice method is the actual slicing of the specimen along the ω -direction. The incident wave enters the specimen at the top, propagates through the specimen and exits at the bottom. In TEM the incident wave is a uniform plane wave traveling in the ω -direction. The specimen is divided into many slices, each of which is thin enough to be approximated as a simple phase shift of the electron beam. The electron beam propagates between slices as a small angle outgoing wave (Fresnel diffraction). The wave is transmitted through a slice of thickness Δz and then propagates a distance Δz along ω to the next layer.

With some mathematical manipulation, outlined in section 3.4, one can utilise the fact that ϕ in (3.4) varies slowly, drop small terms as $\Delta z \to 0$, and arrive at the following expression that is henceforth called the multi-slice equation:

$$\phi(\boldsymbol{x} + \triangle z\boldsymbol{\omega}) = \mathcal{T}_{\triangle z}^{\text{prop}} \Big(\mathcal{T}_{\triangle z}^{\text{trans}}[U](\phi)(\boldsymbol{\omega}, \cdot) \Big)(\boldsymbol{x}) + O(\triangle z^2)$$
(3.5)

for $x \in \mathbb{R}^3$ and $\Delta z > 0$ small. The operators above are given as follows:

Transmission: $\mathcal{T}_{\triangle z}^{\text{trans}}[U](\psi)$ models the *transmission* of a electron wave function $\psi \colon \mathbb{R}^3 \to \mathbb{C}$ through a specimen characterised by its scattering potential $U \colon \mathbb{R}^3 \to \mathbb{C}$, see (3.2). The wave function ψ is transmitted the distance $\triangle z$ from \boldsymbol{x} to $\boldsymbol{x} + \triangle z \boldsymbol{\omega}$ through a specimen along the $\boldsymbol{\omega}$ -direction by means of a phase shift given by a projection of U:

$$\mathcal{T}_{\Delta z}^{\text{trans}}[U](\phi)(\boldsymbol{\omega}, \boldsymbol{x}) := \phi(\boldsymbol{x} + \Delta z \boldsymbol{\omega}) \exp\left[\frac{i}{2k} \int_{0}^{\Delta z} U(\boldsymbol{x} + t \boldsymbol{\omega}) \, dt\right]. \tag{3.6}$$

Propagation: $\mathcal{T}_{\triangle z}^{\text{prop}}(\psi)$ models the *free-space propagation* of a wave function $\psi \colon \mathbb{R}^3 \to \mathbb{C}$ for a distance $\triangle z$. If $\triangle z$ is small enough, the propagated wave can be ap-

proximated through Fresnel diffraction along the ω -direction (section 3.4.1):

$$\mathcal{T}_{\boldsymbol{\omega}, \triangle z}^{\text{prop}}(\phi)(\boldsymbol{x}) := \left\{ P_{\boldsymbol{\omega}, \triangle z} \underset{\boldsymbol{\omega}^{\perp}}{\circledast} \psi \right\} (\boldsymbol{x})$$
 (3.7)

with

$$P_{oldsymbol{\omega}, riangle z}(oldsymbol{x}) := rac{k}{i2\pi riangle z} \exp\Bigl(irac{k}{2 riangle z}ig|oldsymbol{x} - (oldsymbol{x} \cdot oldsymbol{\omega})oldsymbol{\omega}\Bigr|^2\Bigr).$$

Now, let ϕ_n denote the wave function from (3.4) restricted to the n:th slice with thickness Δz , $\omega^{\perp} + n\Delta z\omega$, i.e.

$$\phi_n(\boldsymbol{x}) := \phi(\boldsymbol{x} + n\triangle z\boldsymbol{\omega}) \text{ for } \boldsymbol{x} \in \boldsymbol{\omega}^{\perp}.$$

Then, the multi-slice equation (3.5) can be written recursively as

$$\begin{cases} \phi_0(\boldsymbol{x}) := 1 \\ \phi_{n+1}(\boldsymbol{x}) = \mathcal{T}_{\Delta z}^{\text{prop}} \Big(\mathcal{T}_{\Delta z}^{\text{trans}}[U](\phi_n)(\boldsymbol{\omega}, \cdot) \Big)(\boldsymbol{x}) & \text{for } \boldsymbol{x} \in \boldsymbol{\omega}^{\perp}. \end{cases}$$
 (3.8)

In the above, we have used the convention that ω^{\perp} is the plane orthogonal to ω just before the specimen, so ϕ_0 will be the incoming plane wave used for illumination and

$$\phi_0(\boldsymbol{x}) = \exp(ik\boldsymbol{x} \cdot \boldsymbol{\omega}) = \exp(0) = 1$$
 for all $\boldsymbol{x} \in \boldsymbol{\omega}^{\perp}$.

3.4 Deriving the multi-slice equation

3.4.1 Electrons that mainly propagate along a fixed direction

We here consider the case of high energy imaging electrons that propagate along a "main" direction, which we without loss of generality can set to the z-axis. To be more precise, the idea here is that fast oscillations are mainly along the z-direction. In such case it is natural to write

$$\psi(\mathbf{x}) = \phi(\mathbf{x}) \exp(ikz) \tag{3.9}$$

and ϕ above is slowly varying along z-axis. The extreme case is a plane wave propagating along the z-axis, which corresponds to $\phi \equiv 1$.

Inserting (3.9) into (3.3) gives us

$$-\left[\nabla^2 + U(\boldsymbol{x})\right]\phi(\boldsymbol{x}) = 2ik\frac{\partial}{\partial z}\phi(\boldsymbol{x}). \tag{3.10}$$

3.4. DERIVING THE MULTI-SLICE EQUATION

The above follows from

$$\nabla^{2}\psi = \nabla \cdot \left[\nabla(\phi \exp(ikz))\right] = \nabla \cdot \left[\exp(ikz)\left(\frac{\partial\phi}{\partial x}e_{x} + \frac{\partial\phi}{\partial y}e_{y}\right)\right]$$
$$+ \left(ik \exp(ikz)\phi(x) + \exp(ikz)\frac{\partial\phi}{\partial z}\right)e_{z}$$
$$= \exp(ikz)\left(\frac{\partial^{2}\phi}{\partial x^{2}} + \frac{\partial^{2}\phi}{\partial y^{2}}\right)$$
$$- k^{2} \exp(ikz)\phi + 2ik \exp(ikz)\frac{\partial\phi}{\partial z} + \exp(ikz)\frac{\partial^{2}\phi}{\partial z^{2}}$$
$$= \exp(ikz)\left[\nabla^{2}\phi - k^{2}\phi + 2ik\frac{\partial\phi}{\partial z}\right]$$

where $e_x := (1,0,0), e_y := (0,1,0),$ and $e_z = (0,0,1)$ denote the Cartesian unit vectors. Next, split the Laplacian ∇^2 into a z-directional and a transversal part:

$$\nabla^2 = \nabla_{\perp}^2 + \frac{\partial^2}{\partial z^2}$$
 where $\nabla_{\perp}^2 = \frac{\partial^2}{\partial x^2} + \frac{\partial^2}{\partial y^2}$ (3.11)

and use in (3.10):

$$-\left[\nabla_{\perp}^{2} + U(\boldsymbol{x})\right]\phi(\boldsymbol{x}) = 2ik\frac{\partial}{\partial z}\phi(\boldsymbol{x}) + \frac{\partial^{2}}{\partial z^{2}}\phi(\boldsymbol{x})$$
(3.12)

This far we have not made any approximations, i.e, mathematically (3.3) and (3.12) are equivalent. Our next step is however based on assuming that ϕ varies slowly as compared to k in the sense that

$$\left| 2ik \frac{\partial}{\partial z} \phi(\mathbf{x}) \right| \gg \left| \frac{\partial^2}{\partial z^2} \phi(\mathbf{x}) \right|.$$
 (3.13)

Then (3.12) can be simplified into

$$-\left[\nabla_{\perp}^{2} + U(\boldsymbol{x})\right]\phi(\boldsymbol{x}) \approx 2ik\frac{\partial}{\partial z}\phi(\boldsymbol{x}). \tag{3.14}$$

Note that this equation looks exactly like the time-dependent Schrödinger equation with t substituted with z. There are different rationales for motivating the omission of the $\partial^2 \phi / \partial z^2$ -term in (3.12) and how this is to be interpreted from a physics point-of-view [18, 25, 23, 2].

3.4.2 Free space propagation

The aim of this section is to arrive at an analytical form for wave function of electrons with constant energy given the boundary value on a plane orthogonal to the z-axis. For this purpose we first solve (3.14) for a plane wave with a fixed energy and then show how we can arrive at the case with general boundary condition using superposition of some of these plane waves. This refers to the propagation of the

electron wave in free space, i.e., we seek to solve (3.3) for $U \equiv 0$. From (3.14) we get

$$-\nabla_{\perp}^{2}\phi(\boldsymbol{x}) = 2ik\frac{\partial}{\partial z}\phi(\boldsymbol{x}). \tag{3.15}$$

As in time-dependent Schrödinger equation, in order to solve this equation for a plane wave, we split ϕ into a transversal and a z-directional part:

$$\phi(\mathbf{x}) = \exp(i\mathbf{k}' \cdot \mathbf{x}') \exp(i\mathbf{k}'_z z) \quad \text{where } \mathbf{x}' = (x, y). \tag{3.16}$$

Note that wave numbers of ϕ are noted with a prime to be distinguishable with those of ψ . Splitting ϕ in this form gives a solution which its uniqueness is justified with Sommerfeld radiation condition [31].

Substituting (3.16) into the left-hand-side of (3.15) gives us

$$-\nabla_{\perp}^{2}\phi(\boldsymbol{x}) = -\nabla \cdot \nabla \left[\exp(i\boldsymbol{k}' \cdot \boldsymbol{x}') \exp(ik'_{z}z)\right]$$

$$= -\nabla \cdot \left[i(k'_{x}\boldsymbol{e}_{x} + k'_{y}\boldsymbol{e}_{y}) \exp(i\boldsymbol{k}' \cdot \boldsymbol{x}') \exp(ik'_{z}z)\right]$$

$$= (k'^{2}_{x} + k'^{2}_{y}) \exp(i\boldsymbol{k}' \cdot \boldsymbol{x}') \exp(ik'_{z}z) = |\boldsymbol{k}'|^{2}\phi(\boldsymbol{x}).$$

Similarly, the right-hand-side of (3.15) gives us

$$2ik\frac{\partial}{\partial z}\phi(\mathbf{x}) = 2ik(ik_z')\exp(i\mathbf{k}'\cdot\mathbf{x}')\exp(ik_z'z) = -2kk_z'\phi(\mathbf{x}).$$

Hence,

$$|\mathbf{k}'|^2 \phi(\mathbf{x}) = -2kk_z' \phi(\mathbf{x}) \iff -|\mathbf{k}'|^2 = 2kk_z' \iff k_z' = -\frac{|\mathbf{k}'|^2}{2k}.$$

Inserting this value for k'_z into (3.16) gives us the solution

$$\phi(\mathbf{x}', z) = \exp(i\mathbf{k}' \cdot \mathbf{x}') \exp\left(-i\frac{|\mathbf{k}'|^2}{2k}z\right). \tag{3.17}$$

As a final note, let us consider (3.13). Its left-hand-side is

$$\left|2ik\frac{\partial}{\partial z}\phi(\boldsymbol{x})\right| = \left|-2kk_z'\phi(\boldsymbol{x})\right| = 2k|k_z'|\phi(\boldsymbol{x})|$$

and its right-hand-side is

$$\left|\frac{\partial^2}{\partial z^2}\phi(\boldsymbol{x})\right| = \left|(ik_z')^2\phi(\boldsymbol{x})\right| = |k_z'|^2 |\phi(\boldsymbol{x})|.$$

Hence, (3.13) reads as

$$2k|k_z'||\phi(\boldsymbol{x})| \gg |k_z'|^2|\phi(\boldsymbol{x})| \iff 2k \gg |k_z'| \iff 4k^2 \gg |\boldsymbol{k}'|^2$$

The last equivalent formulation above comes from using $k'_z = -|\mathbf{k}'|^2/2k$. Now, k just represents the total energy of the particle. The kinetic energy and direction of propagation can vary with very small amounts and angles. We see that $4k^2 \gg |\mathbf{k}'|^2$ is required for propagation direction to be close to the z-direction.

3.4. DERIVING THE MULTI-SLICE EQUATION

General case: Equation (3.14) and (3.10) are linear in terms of ϕ . Hence, let ϕ_1 and ϕ_2 be two solutions under two different boundary conditions ϕ_1^b and ϕ_2^b . Then, the solution under the boundary condition $\alpha \phi_1^b + \beta \phi_1^b$ is $\alpha \phi_1 + \beta \phi_2$. This statement could be restated in terms of the linear operator $\mathcal{A}_{\Delta z}$ which maps a function ϕ_{in} on the (\mathbf{x}', z_0) -plane to a function ϕ_{out} on the $(\mathbf{x}', z_0 + \Delta z)$ -plane in which

$$\phi_{\text{out}}(\boldsymbol{x}') := \phi(\boldsymbol{x}', z_0 + \Delta z),$$

so both input and output of this system are two dimensional functions of x'. Hence,

$$\mathcal{A}_{\Delta z}(\phi_{\mathrm{in}})(\boldsymbol{x}') = \phi_{\mathrm{in}}(\boldsymbol{x}')$$

From (3.17) we can conclude that if ϕ is a plane wave then $\phi_{\rm in}$ and $\phi_{\rm out}$ contain only one frequency in \boldsymbol{x}' -plane which is $\boldsymbol{\xi} = \boldsymbol{k}'/2\pi$, and we can write:

$$\phi_{\text{out}}(\mathbf{x}') = \phi_{\text{in}}(\mathbf{x}') \exp\left(-i\frac{|\mathbf{k}'|^2}{2k}\Delta z\right)$$
(3.18)

This equation introduces a single frequency analysis for operator $\mathcal{A}_{\Delta z}$ in the sense that

$$\mathbf{k}' \mapsto \exp\left(-i\frac{|\mathbf{k}'|^2}{2k}\Delta z\right)$$

is the frequency response (also known as transfer function) at the frequency $\boldsymbol{\xi} = \boldsymbol{k}'/2\pi$. Substituting this value for $\boldsymbol{\xi}$ we can rewrite the frequency response as:

$$H(\boldsymbol{\xi}) := \exp\left(-i\frac{|2\pi^2\boldsymbol{\xi}|^2}{k}\Delta z\right) \tag{3.19}$$

Generally $\phi_{\rm in}$ and $\phi_{\rm out}$ could be expressed through the Fourier transform:

$$\phi_{\rm in}(\mathbf{x}') = \iint \Phi_{\rm in}(\boldsymbol{\xi}) \exp(i2\pi\boldsymbol{\xi} \cdot \mathbf{x}') \,\mathrm{d}\boldsymbol{\xi}$$
 (3.20)

$$\phi_{\text{out}}(\boldsymbol{x}') = \iint \Phi_{\text{out}}(\boldsymbol{\xi}) \exp(i2\pi\boldsymbol{\xi} \cdot \boldsymbol{x}') \,\mathrm{d}\boldsymbol{\xi}$$
 (3.21)

where

$$\Phi_{\rm in}(\boldsymbol{\xi}) = \iint \phi_{\rm in}(\boldsymbol{x}') \exp(-i2\pi \boldsymbol{x}' \cdot \boldsymbol{\xi}) \, \mathrm{d}\boldsymbol{x}'$$
 (3.22)

$$\Phi_{\text{out}}(\boldsymbol{\xi}) = \iint \phi_{\text{out}}(\boldsymbol{x}') \exp(-i2\pi \boldsymbol{x}' \cdot \boldsymbol{\xi}) \, d\boldsymbol{x}'. \tag{3.23}$$

Knowing the frequency response, we can write the relationship between Φ_{in} and Φ_{out} as:

$$\Phi_{\text{out}}(\boldsymbol{\xi}) = \Phi_{\text{in}}(\boldsymbol{\xi})H(\boldsymbol{\xi}). \tag{3.24}$$

We can now explicitly calculate the inverse Fourier transform of H:

$$\check{H}(\mathbf{x}') = \frac{k}{i2\pi\Delta z} \exp\left(\frac{ik|\mathbf{x}'|^2}{2\Delta z}\right).$$

Thus, (3.24) can be restated in real space as a 2D-convolution:

$$\phi_{\mathrm{out}}(\boldsymbol{x}') = \frac{k}{i2\pi\Delta z} \Big\{ \phi_{\mathrm{in}} \otimes \exp\Big(\frac{ik|\cdot|^2}{2\Delta z}\Big) \Big\} (\boldsymbol{x}').$$

In summary, slowly varying part ϕ of the electron wave ψ is, after propagating a distance Δz in free space, given as

$$\phi(\mathbf{x}', z + \Delta z) = \{\phi(\cdot, z) \otimes P_{\Delta z}\}(\mathbf{x}')$$
(3.25)

where

$$P_{\Delta z}(\mathbf{x}') := \frac{k}{i2\pi\Delta z} \exp\left(i\frac{k}{2\Delta z}|\mathbf{x}'|^2\right).$$

This convolution is called *Fresnel diffraction* and P is often called *Fresnel propagator*. Also, the above expression for ϕ at the $(\mathbf{x}', z + \Delta z)$ -plane is the same as the one given by $\mathcal{T}_{\boldsymbol{\omega}, \Delta z}^{\text{prop}}$ in (3.7) for the case when $\boldsymbol{\omega} = (0, 0, 1)$.

3.4.3 The multislice equation

The material here is based on section 6.4 in [20]. The starting point is to write (3.14) in operator form:

$$\frac{\partial \phi}{\partial z}(x) = [\mathcal{A} + \mathcal{B}(x)](\phi)(x)$$

where

$$\mathcal{A}(\phi)(\ \cdot\):=\frac{i}{2k}\nabla_{\perp}^2\phi(\ \cdot\)\quad \text{and}\quad \mathcal{B}(\boldsymbol{x})(\phi)(\ \cdot\):=\frac{i}{2k}U(\boldsymbol{x})\phi(\ \cdot\).$$

Next, one can express the solution of (3.14) as

$$\phi(\mathbf{x}) = \exp\left[\int_0^z \mathcal{A} + \mathcal{B}(\mathbf{x}', s) \, \mathrm{d}s\right](\phi)(\mathbf{x}', 0)$$
(3.26)

where the above exponential of an operator is defined in terms of a formal series expansion. Offsetting the initial value to z gives us

$$\phi(\mathbf{x}', z + \Delta z) = \exp\left[\int_{z}^{z+\Delta z} \mathcal{A} + \mathcal{B}(\mathbf{x}', s) \, \mathrm{d}s\right](\phi)(\mathbf{x}', z),$$

or equivalently

$$\phi(\mathbf{x}', z + \Delta z) = \exp\left[\int_{z}^{z + \Delta z} \frac{i}{2k} \nabla_{\perp}^{2} + \frac{i}{2k} U(\mathbf{x}', s) \, \mathrm{d}s\right] (\phi)(\mathbf{x}', z)$$

$$= \exp\left[\frac{i}{2k} \Delta z \nabla_{\perp}^{2} + \frac{i}{2k} \int_{z}^{z + \Delta z} U(\mathbf{x}', s) \, \mathrm{d}s\right] (\phi)(\mathbf{x}', z).$$
(3.27)

3.4. DERIVING THE MULTI-SLICE EQUATION

It can now be shown, see [20, p. 133], that the operator in the right-hand-side of (3.26) can be written as a composition of two operators:

$$\exp\left[\int_{z}^{z+\Delta z} \mathcal{A} + \mathcal{B}(\boldsymbol{x}', s) \, \mathrm{d}s\right]$$

$$= \exp\left[\int_{z}^{z+\Delta z} \mathcal{A} \, \mathrm{d}s\right] \circ \exp\left[\int_{z}^{z+\Delta z} \mathcal{B}(\boldsymbol{x}', s) \, \mathrm{d}s\right] + O(\Delta z^{2}). \quad (3.28)$$

In the above, the error of the approximation is of order Δz^2 and goes to zero faster than the first term, hence this guarantees the convergence of the approximation when $\Delta z \to 0$. Note also that the two terms in the right-hand-side above can be exchanged, but since the operators \mathcal{A} and $\mathcal{B}(x)$ do not commute, this would result in a different approximation.

We now start by deriving the expression for $\exp\left[\int_z^{z+\Delta z} \mathcal{A} \, \mathrm{d}s\right]$. When it acts on ϕ , it results in the formal solution to the differential equation

$$\frac{\partial \phi}{\partial z} = \mathcal{A}(\phi).$$

This equation is identical to (3.15) and its solution is given by (3.25), i.e.,

$$\phi(\mathbf{x}', \Delta z) = \{ P_{\Delta z} \otimes \phi(\cdot, z) \} (\mathbf{x}')$$

where

$$P_{\Delta z}(\mathbf{x}') = \frac{k}{i2\pi\Delta z} \exp\left(i\frac{k}{2\Delta z}|\mathbf{x}'|^2\right).$$

In summary, we have that

$$\exp\left[\int_{z}^{z+\Delta z} \mathcal{A} \, \mathrm{d}s\right](\phi) = \exp\left[\int_{z}^{z+\Delta z} \frac{i}{2k} \nabla_{\perp}^{2} \, \mathrm{d}s\right](\phi) = P_{\Delta z} \otimes \phi(\cdot, z). \tag{3.29}$$

Next, we want to calculate $\exp\left[\int_z^{z+\Delta z} \mathcal{B}(x',s) \,\mathrm{d}s\right]$. Inserting the definition of \mathcal{B} and using the expression for U in (3.3) gives us

$$\exp\left[\int_{z}^{z+\Delta z} \mathcal{B}(\boldsymbol{x}',s) \, \mathrm{d}s\right] = \exp\left[\frac{i}{2k} \int_{z}^{z+\Delta z} U(\boldsymbol{x}',s) \, \mathrm{d}s\right]$$
$$= \exp\left[\frac{iem}{k\hbar^{2}} \int_{z}^{z+\Delta z} V(\boldsymbol{x}',s) \, \mathrm{d}s\right] = \exp[i\sigma V_{\Delta z}(\boldsymbol{x}',z)]$$

where

$$V_{\Delta z}(\boldsymbol{x}',z) := \int_z^{z+\Delta z} V(\boldsymbol{x}',s) \,\mathrm{d}s \quad ext{and} \quad \sigma := rac{me}{k\hbar^2} = rac{2\pi me\lambda}{h^2}.$$

In summary, we have that

$$\exp\left[\int_{z}^{z+\Delta z} \mathcal{B}(\boldsymbol{x}',s) \,ds\right](\phi)(\boldsymbol{x}) = \phi(\boldsymbol{x}) \exp[i\sigma V_{\Delta z}(\boldsymbol{x}',z)]. \tag{3.30}$$

CHAPTER 3. ELECTRON-SPECIMEN MODEL

Thus, the final expression for (3.27) is obtained by substituting (3.30) and (3.29) into (3.28):

$$\exp\left[\int_{z}^{z+\Delta z} \mathcal{A} + \mathcal{B}(\boldsymbol{x}',s) \, \mathrm{d}s\right] \approx \left[P_{\Delta z} \otimes\right] \circ \left[\exp(i\sigma V_{\Delta z}(\boldsymbol{x}',z))\right]$$

when Δz is very small. The multi-slice equation (3.5) now follows from inserting the above into (3.27).

Chapter 4

Implementation

The multislice method outlined in section 3.4.3 is implemented in the software package TEM-simulator [29]. This chapter describes the implementation and integration of the multislice method into the TEM-simulator software suite.

4.1 The parts of the TEM-simulator

From a functionality viewpoint, the software components that make up the TEM-simulator can be grouped into two major components:

- 1. Phantom generator: Software allowing the user to generate a synthetic specimen (mathematical phantom) that can be used by the TEM simulator in order to generate a synthetic image.
- 2. *TEM simulator*: Software allowing the user to simulate TEM imaging of the phantom.

4.1.1 Phantom generator

A phantom generator allows a user to specify *which* specimen that is to be modelled and then to assemble a *model of the specimen* that can be used in simulating TEM images. In TEM-simulator, a biological specimen is specified through the following three parts:

- 1. Particles: This is a specification of the molecules (or molecular assemblies) that will be embedded in the background. Each particle is specified at atomic level by a single file in the RCSB Protein Data Bank (PDB) format.
- 2. Background: This is the specification of the background environment encapsulating the particles. The background is modelled as a continuum medium and is assumed to be a slab of aqueous buffer with flat or curved surfaces. The scattering potential for the background is calculated using an averaging procedure, so it is constant.

3. Particle distribution: For each particle, one must provide a specification of its "distribution" in the specimen, i.e., how it is to be distributed in the background environment. It can either be randomly placed in a manner that corresponds to a given concentration, or it can be placed following a specific distribution.

Given the above, the phantom generator will create a mathematical model of a specimen relevant for TEM imaging. This is equivalent to generating the scattering potential U (see (3.2)) of the entire specimen given a specification of the background, particles, and the distribution of the particles in the background. This involves difficulties such as how to fuse the scattering potentials of the particles with that of the background, how to model the natural granularity of the background, and at what resolution (in terms of sampling) to represent the phantom. How these issues are handled is described in [29].

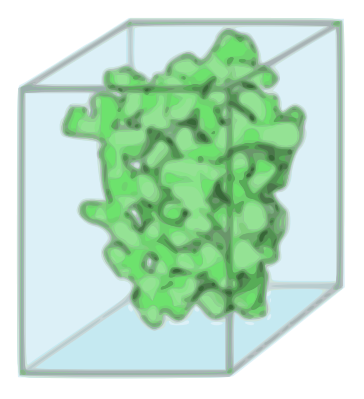


Figure 4.1. A particle stored in a three dimensional array.

4.1.2 TEM simulator

TEM simulator starts with a plane wave representing the wave function of electrons leaving the condenser. It induces the interaction effect of the specimen's electrostatic potential on the wave function by means of linear or multislice method described in section 3.3. It then applies the linear influence of the lens and partial incoherence due to incoherent illumination. The wave function then takes the effect of the detector and its intensity is calculated and noise is added. The intensity received by each element on the detector's matrix represents the pixelized digital image which is saved on an MRC file.

4.2 Steps of the multislice method

In the multislice method, the specimen is first sub-divided into thin slabs of thickness Δz . The two parallel hyperplanes that demarcate each slab are orthogonal to the propagation of the incident electron. Next, for each slab the wave at the upper slab is first phase shifted by an amount proportional to the projection of the scattering potential (transmission), and then it is propagated a distance of Δz to the lower slab (propagation). This is expressed by formulas in (3.8).

4.2.1 Wave function

The wave function basically is a two dimensional array that holds the complex numbers that represent the values of the sampled wave function traveling through different components of electron microscope. Its pixel size is equal to pixel size of the detector divided by magnification, and its size is the same as that of the detector; considering that wave function is to be sampled by the detector, therefore the best sampling rate for the wave function is the one matching the detector's pixel size.

4.2.2 Generating slices

Following the representation of a specimen in the TEM-simulator, its scattering potential is given by

$$V(\boldsymbol{x}) = \sum_{q=1}^{m} \sum_{r} V_q((\boldsymbol{x} - \boldsymbol{x}_{q,r}) \cdot \boldsymbol{R}_{q,r}).$$
 (4.1)

In the above, m is the number of the particle types, $x_{q,r}$ is the position of the r-th copy of the q-th particle, and $R_{q,r}$ is the 3×3 -transformation matrix of that particle associated with its orientation, and $V_q(x)$ is the scattering potential of q-th particle at x. Its origin is the center of the particle and it is zero outside the range of electrostatic potential of the molecule.

For creating slices, there is a block of memory allocated representing a three dimensional slice. Its length, width and voxel size are determined by the detector's dimension and pixel size just like wave function. The thickness (size along the beam direction) of this box depends on the slice thickness which is determined by user. In each step of multislice method, a slice of specimen is generated and stored in this block of memory.

Having the orientation and position of all particles in a table, the software fills in the voxels of the slice with the complex values of the electro statistic potential of space inside the slice. Trilinear interpolation is used to derive the potential of the voxels from the slice which are falling inside a particle. Figure 4.2 roughly shows how the voxels of a particle is positioned relative to the voxels of slice. The rest of the voxels either equal to potential of buffer (4.877 + i0.824 V) if they exist inside the buffer or zero if they do not. Geometry of buffer is shown in the figure 4.3.

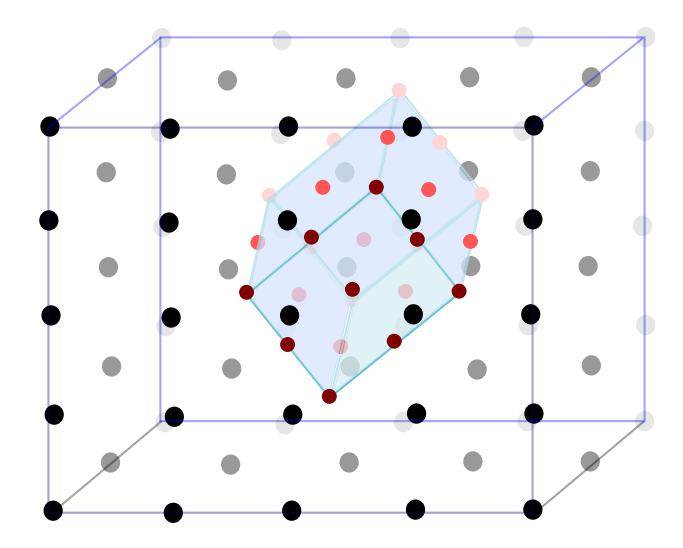


Figure 4.2. Tri-linear interpolation is used to calculate the voxel values of one slice (black dots) from the known voxel values of a particle existing inside the slice (red dots).

4.2.3 Propagation

Propagation is the numerical implementation of Fresnel diffraction of the wave function along the beam direction. Hence we need to calculate the convolution between the wave function and the Fresnel propagator,

$$(\boldsymbol{x}',z)\mapsto rac{1}{i\lambda\Delta z}\exp\Bigl(rac{i\pi}{\lambda\Delta z}|\boldsymbol{x}'|^2\Bigr).$$

The convolution changes into a multiplication in the Fourier space. To calculate this multiplication in the discrete Fourier space, FFT is used to take the discrete wave function to the Fourier space. For the propagator though, sampling is applied to the analytically Fourier-transformed of the Fresnel propagator 3.19. The frequency components of the propagator that correspond to higher frequencies than the wave function's Nyquist frequency (half of the sampling rate), are canceled out in the multiplication; hence no aliasing effect due to under-sampling will occur; un-

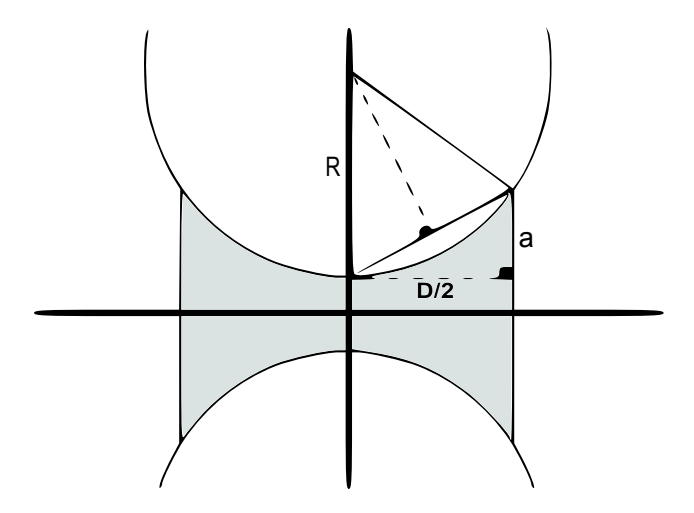


Figure 4.3. Buffer's geometry. $R = \frac{a^2 + (D/2)^2}{2a}$

like the case where we want to calculate the convolution directly in the discrete real space. In the end, the product is transformed back to the real space using inverse FFT.

In conclusion, what is done here is a simple multiplication of the Discrete Fourier Transform (DFT) transformed of the wave function by sampled data of the function

$$(\xi_1, \xi_2) \mapsto \exp\left[-i2\pi^2 z(\xi_1^2 + \xi_2^2)/k\right]$$

and ultimately DFT inverse transform the result.

$$\psi_n^P(i,j) := DFT^{-1} \{ DFT \{ \psi_{n-1}^P \} \mathcal{T}_{2D} \left(\exp\left[-i2\pi^2 z(\xi_1^2 + \xi_2^2)/k \right] \right)$$
(4.2)

 \mathcal{T}_{2D} is two dimensional sampling with the same sampling frequency equal to that of the wave function ψ .

4.2.4 Transmission

In this step the projection of the slice is calculated along the z axis². This projection is a simple summation of voxels that stand contiguous along the z axis. The wave

¹This sampled data should be arranged somehow to follow the DFT's frequency pattern where the lowest frequencies are in the corners and the highest are in the middle of the image.

²In the Simulation in every tilt mode, the propagation axis remains constant and the specimen is rotated respectively.

function is then phase-shifted in the corresponding pixels based on the equation 3.30:

$$\psi_n(i,j) := \psi_n^P(i,j) \exp(i\sigma\mu_P \sum_k V(i,j,k))$$
(4.3)

where ψ_n is the wave function after transmission and ψ_n^P is the wave function after propagation. V is discretized scattering potential of the slice and μ_p is its voxel size.

4.2.5 Optics and Detectors

After sequential propagation and transmission for all of the slices, we apply CTF effect. The true defocus value is determined by adding the nominal defocus given by the user and the level where outgoing wave function exists the specimen which is equal to half of the specimen's thickness ³. In the next step the intensity of the wave is measured and noise is added in the detector and its written on an MRC file. In these steps the original methods and functions in TEM-Simulator 1.3 are used.

4.3 Modifications in TEM-Simulator

The multislice method is integrated in the new release of TEM-Simulator (version 1.4). User can select between three different options of electron-specimen model. With multislice being selected as the model of interaction, the slice thickness can be set to a value which determines the precision of the model.

List of modified files:

TEM-simulator.c; The main function exists in this file which handles input management. This file is modified to view the documentation of the added features by executing 'TEM-simulator -help'.

simulation.c; it contains the main algorithm of the whole simulation and controls the mode of interaction which is modified to be able to navigate between different modes.

multislice.c is added and it contains the functions necessary for calculating the slice, projection, and propagation as well as the function that performs the algorithm of multislice method.

³In the "projection" mode this addition to defocus value is not needed.

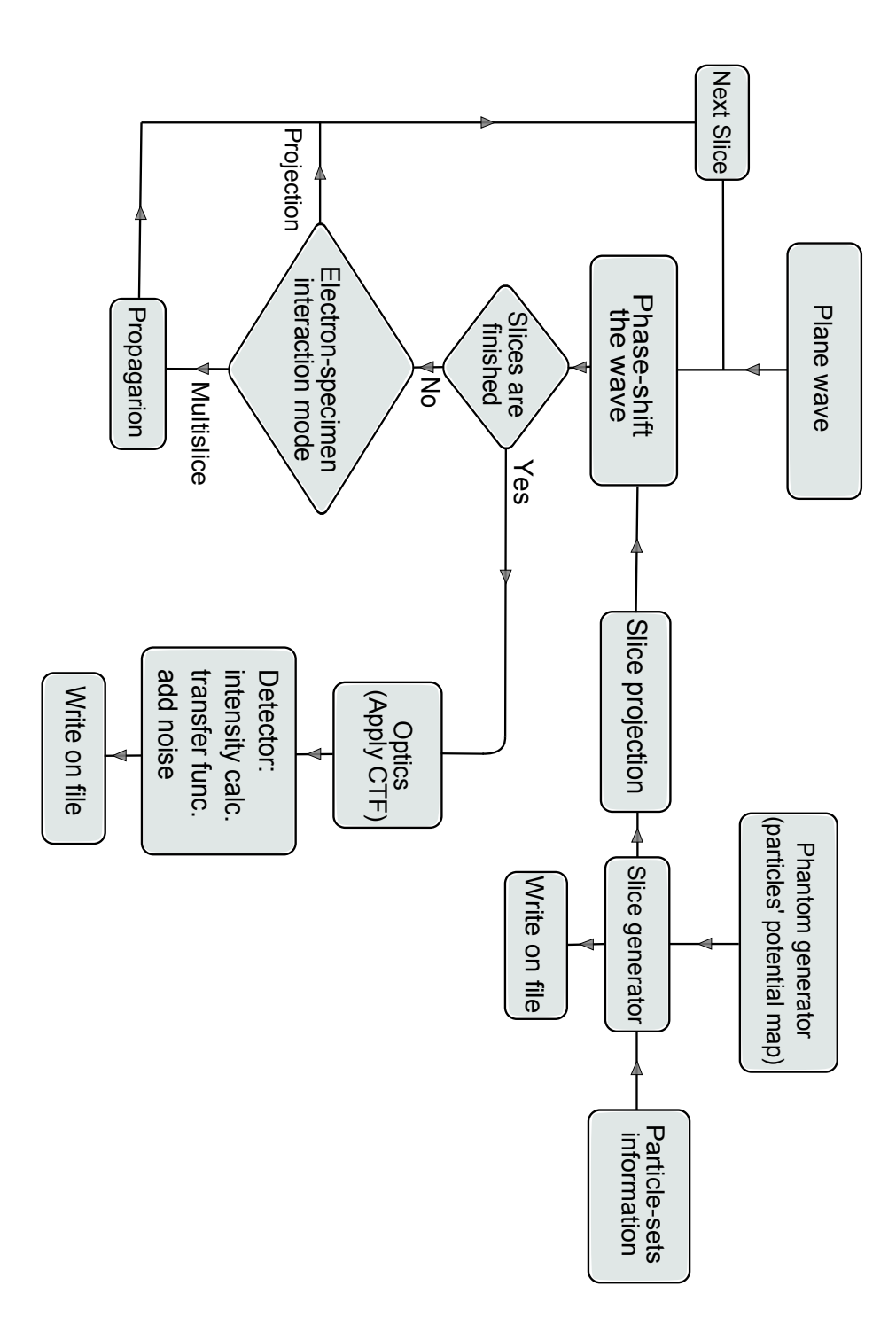


Figure 4.4. Flowchart of the program in multislice or projection mode.

Chapter 5

Results

Here we summarise the results from tests of implemented multislice method using TEM simulator. For the test we used an *in vitro* sample containing Ribonucleic Acid (RNA) polymerase particles and spherical gold particles. The RNA polymerase is a molecular complex that is fairly well characterised from structural point of view (figure 5.2(a)) and figure 5.1 shows this molecular complex in different orientations.

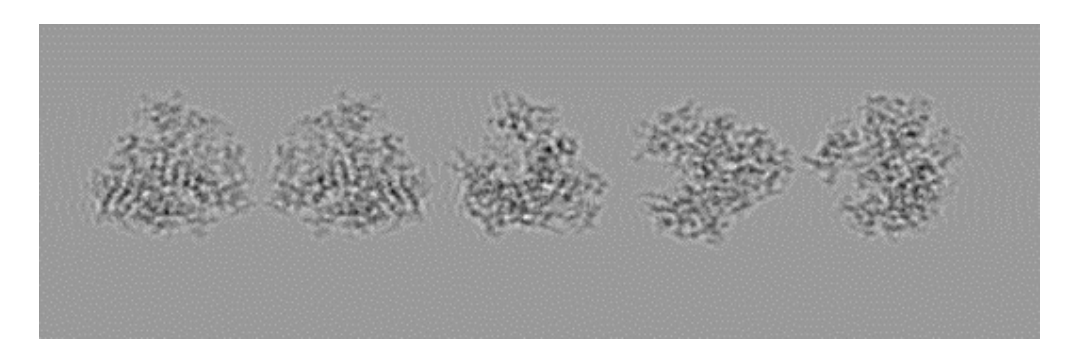
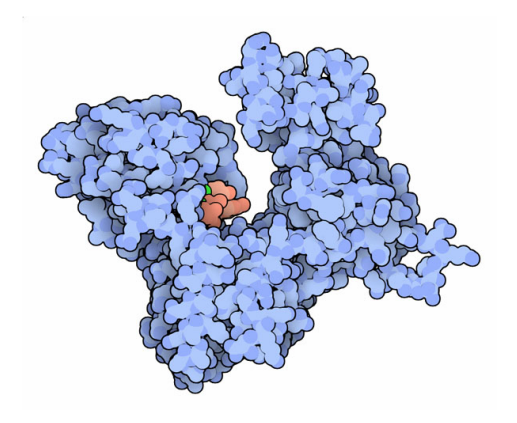
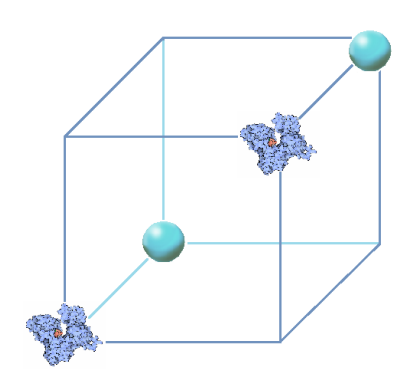


Figure 5.1. RNA polymerase with random orientations

To test the propagation part of the multislice method, two pairs of identical particles are placed at different levels along the propagation axis. The relative positions of the particles are shown in figure 5.2(b). We should be able to set the focus on both levels. This test confirms that the propagation in the multislice method is consistent with the optic point spread effect due to defocus. The results of this test is shown in figure 5.3. In figure 5.3(a) focus is on the right side particles which means the left side particles are over-focused. In this image we can see the focused particles with higher detail but lower contrast. In figure 5.3(b), defocus is set somehow that left particles are in-focus and right side particles are underfocused, consequently, we can clearly observe the difference between over-focus and under-focus effects in these images which is consistent with CTF transform function with defocus values greater and lower than zero.



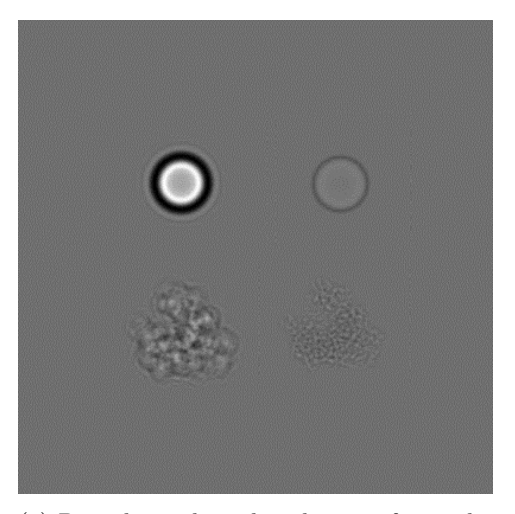


- (a) The RNA polymerase particle.
- (b) Positions of the RNA polymerase and gold particles.

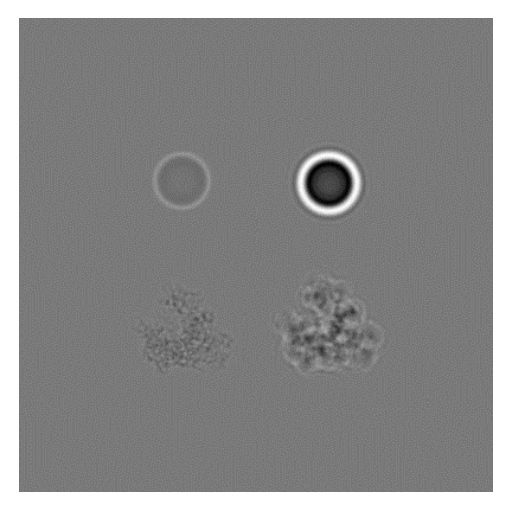
Figure 5.2. Specimen consists of two pairs of identical RNA polymerase and gold particles. The RNA polymerase is shown in figure (a). The placement of the RNA polymerase and gold particles are at different levels along the propagation axis, see figure (b).

In the next test we are comparing the projection approximation with multislice. The same particles with the same positions are used. The defocus value is zero. one time the interaction mode is set to *multislice* and another time it is set to *projection* mode. Figure 5.4(a) is obtained in *multislice* mode. We can see that one pair of particles are under-focused and the other pair are over-focused while in Figure 5.4(b) where the mode is *projection*, there is no difference between particles in the image although they are at different levels.

In the next test we form a complete specimen by particles with random positions and orientations and buffer with thickness variation, with and without noise in the detector.

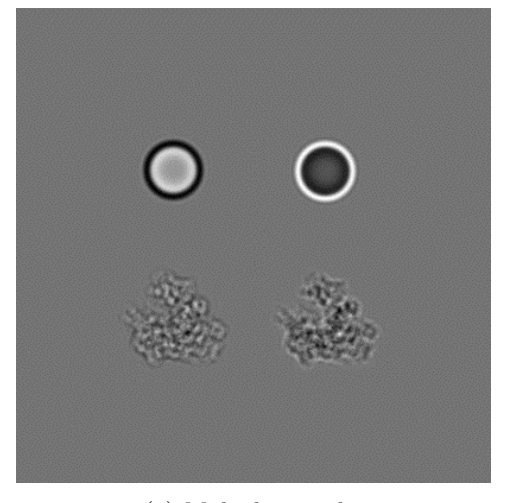


(a) Particles in the right side are in focus, the ones in the left side are $630~\mathrm{nm}$ over-focused.

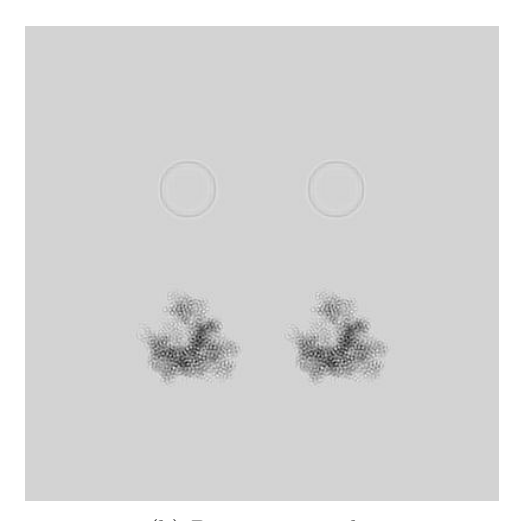


(b) Particles in the right side are in focus, the ones in the left side are 630 nm underfocused.

Figure 5.3. Examples of comparisons of images at 630 nm under-focus (a) and over-focus (b) against corresponding images taken in focus.

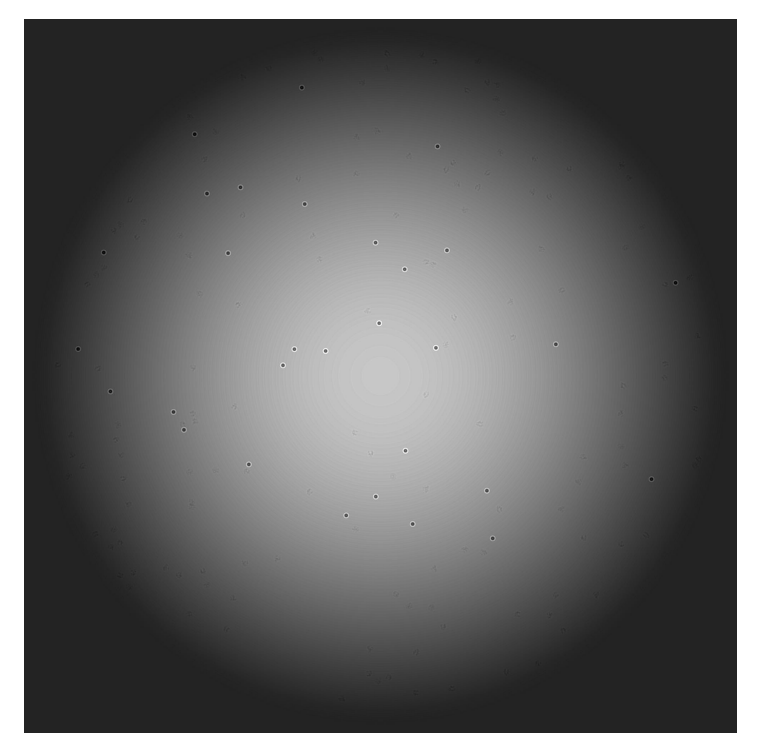


(a) Multislice mode.

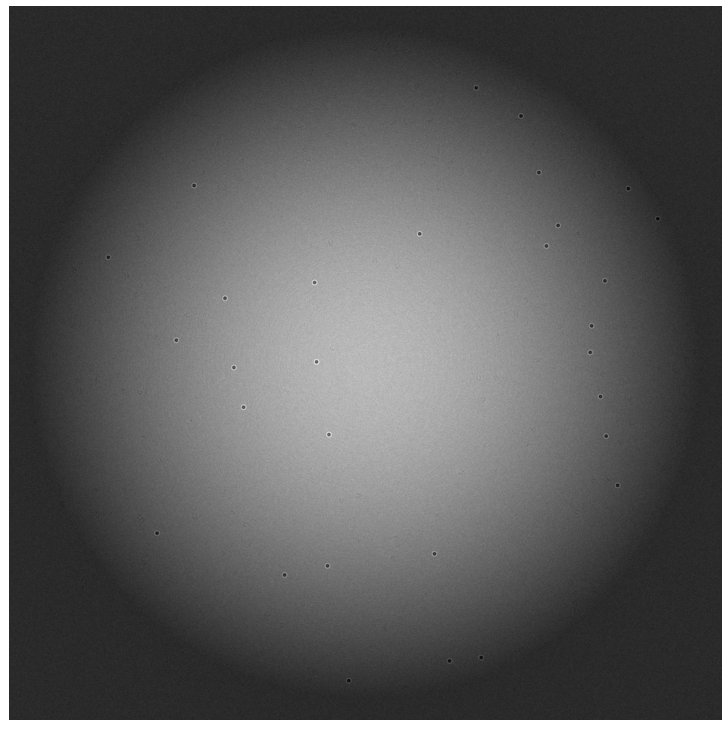


(b) Projection mode.

Figure 5.4. Comparison of images simulated using multislice and projection. Images simulate TEM imaging at zero defocus. Multislice mode is shown in (a) and projection mode is shown in (b).



(a) Noise-free TEM image.



(b) TEM image with noise.

Figure 5.5. TEM image of a specimen with RNA polymerase particles taken at 3 μm under-focus.

Bibliography

- A. Al-Amoudi, J-J. Chang, A. Leforestier, A. McDowall, L. M. Salamin, L. P. O. Norlén, K. Richter, N. S. Blanc, D. Studer, and J. Dubochet. Cryoelectron microscopy of vitreous sections. *EMBO Journal*, 23:3583–3588, 2004.
- [2] D. M. Bird. Theory of zone axis electron diffraction. *Journal of Electron Microscopy Technique*, 13(2):77–97, 1989.
- [3] L. A. Bursill and A. R. Wilson. Electron-optical imaging of the hollandite structure at 3å resolution. *Acta Crystallographica Section A: Foundations of Crystallography*, 33:672—676, 1977.
- [4] J. M. Cowley and A. F. Moodie. The scattering of electrons by atoms and crystals. i. a new theoretical approach. *Acta Crystallographica*, 10(10):609–619, 1957.
- [5] M. De Graf. Introduction to Conventional Transmission Electron Microscopy. Cambridge University Press, Cambridge, UK, 2003.
- [6] H. P. Erikson. The Fourier transform of an electron micrograph first order and second order theory of image formation. Advances in Optical and Electron Microscopy, 5:163–199, 1973.
- [7] P. L. Fejes. Approximations for the calculation of high resolution electron microscope images of thin films. *Acta Crystallographica Section A*, A33:109–113, 1977.
- [8] J. Frank. The envelope of electron microscope transfer functions for partially coherent illumination. *Optik*, 38:519–536, 1972.
- [9] J. Frank. Single-particle reconstruction of biological macromolecules in electron micrscopy 30 years. Quarterly Review of Biophysics, 42:139–158, 2009.
- [10] K. Fujiwara. Relativistic dynamical theory of electron diffraction. *Journal of the Physical Society of Japan*, 16:2226–2238, 1961.
- [11] R. M. Glaeser, K. H. Downing, D. DeRozier, W. Chu, and J. Frank. *Electron Crystallography of Biological Macromolecules*. Oxford University Press, 2006.

- [12] A. Gómez-Rodríguez, L. M. Beltrán-del Río, and R. Herrera-Becerra. SimulaTEM: Multislice simulations for general objects. *Ultramicroscopy*, 110:95–104, 2010.
- [13] P. Goodman and A. F. Moodie. Numerical evaluations of n-beam wave functions in electron scattering by the multi-slice method. Acta Crystallographica Section A, 30(2):280–290, 1974.
- [14] F. Haguenau, P. W. Hawkes, J. L. Hutchison, B. Satiat-Jeunemaître, G. T. Simon, and D. B. Williams. Key events in the history of electron microscopy. *Microscopy and Microanalysis*, 9:96—138, 2003.
- [15] K. J. Hanszen. The optical transfer theory of the electron microscope: fundamental principles and applications. Advances in Optical and Electron Microscopy, 4:1–84, 1971.
- [16] R. Henderson. Realizing the potential of electron cryo-microscopy. *Quarterly Review of Biophysics*, 37:3–13, 2004.
- [17] W. Hoppe. Principles of electron structure research at atomic resolution using conventional electron microscopes for the measurement of amplitudes and phases. *Acta Crystallographica Section A*, A26(4):414–426, 1970.
- [18] A. Howie and Z. S. Basinski. Approximations of the dynamical theory of diffraction contrast. *Philosophical Magazine*, 17(149):1039–1063, 1968.
- [19] K. Ishizuka and N. Uyeda. A new theoretical and practical approach to the multislice method. Acta Crystallographica Section A: Foundations of Crystallography, 33:740—749, 1977.
- [20] E. J. Kirkland. Advanced Computing in Electron Microscopy. Springer Verlag, 2nd edition, 2010.
- [21] A. Leis, B. Rockel, L. Andrees, and W. Baumeister. Visualizing cells at the nanoscale. *Trends in biochemical sciences*, 34(2):60–70, 2009.
- [22] F. A. Lenz. Transfer of image information in the electron microscope. In U. Valdre, editor, *Electron microscopy in materials science*, pages 541–569. Academic Press, 1971.
- [23] A. L. Lewis, R. B. Hammond, and R. E. Villagrana. The importance of secondorder partialderivatives in the theory of high-energy-electron diffraction from imperfect crystals. *Acta Crystallographica Section A*, A31(2):221–227, 1975.
- [24] V. Lucic, F. Forster, and W. Baumeister. Structural studies by electron tomography: from cells to molecules. Annual Review of Biochemistry, 74:833—865, 2005.

BIBLIOGRAPHY

- [25] D. F. Lynch and A. F. Moodie. Numerical evaluation of low energy electron diffraction intensities: I. The perfect crystal with no upper layer lines and no absorption. the perfect crystal with no upper layer lines and no absorption. Surface Science, 32(2):422–438, 1972.
- [26] R. McIntosh, D. Nicastro, and D. Mastronarde. New views of cells in 3D: an introduction to electron tomography. *Trends Cell Biolology*, 15:43–51, 2005.
- [27] L. M. Peng, S. L. Dudarev, and M. J. Whelan. *High Energy Electron Diffraction and Microscopy*. Oxford University Press, 2004.
- [28] C. V. Robinson, A. Sali, and W. Baummeister. The molecular sociology of the cell. *Nature*, 450:973–982, 2007.
- [29] H. Rullgård, L.-G. Öfverstedt, S. Masich, B. Daneholt, and O. Öktem. Simulation of transmission electron microscope images of biological specimens. *Journal of Microscopy*, 243(3):234–256, 2011.
- [30] O. Scherzer. The theoretical resolution limit of the electron microscope. *Journal of Applied Physics*, 20:20–29, 1949.
- [31] A. Sommerfeld. Partial Differential Equations in Physics. Academic Press, 1949.
- [32] A. C. Steven and W. Baummeister. The future is hybrid. *Journal of Structural Biology*, 163:186–195, 2008.
- [33] F. Thon. Phase contrast electron microscopy. In U. Valdre, editor, *Advances in Optical and Electron Microscopy*, pages 571–625. Academic Press, 1971.
- [34] R. H. Wade and J. Frank. Electron microscope transfer functions for partially coherent axial illumination and chromatic defocus spread. *Optik*, 49:81–92, 1977.
- [35] D. B. Williams and C. B. Carter. *Transmission Electron Microscopy*. Springer Verlag, 1996.